Chapter II

Synthesis and basic characterization of Gd_2O_3 and $GdVO_4$ nanosystems

2.1. Gd_2O_3 nanoparticles and nanorods: Citrate-gel and Hydrothermal route

2.1.1. Processing of Gd_2O_3 nanosystems via citrate-gel route

Unlike many other oxides which are comparatively easy to synthesize, nanometric REOs seek appropriate routes owing to their excellent chemical and mechanical stability. In fact, top-down approaches, which generally rely on crushing and smashing are never easy for the REO yielding its nanoscale form. Nevertheless, allowing aggregation of molecular species combined with the formation of a less-stable hydroxide form, and subsequent reduction to its oxide form is an attractive means in the bottom-up approach. Here, nanoscale Gd_2O_3 product is derived through a citrate-gel method following relevant steps described elsewhere [1, 2], but with slight modifications. At first, gadolinium acetate (GdAc) [$Gd(CH_3CO_2)_3$, CDH, 99.9% pure] is dispersed in millipore® (deionized, DI) water followed by preparation of a equimolar solution with the addition of citric acid (CDH, 99% pure) under vigorous stirring (~300 rpm, 30min). Then the as-received gel-like mixture was placed carefully in a hot-air oven, maintaining a temperature of 90^oC. The annealing process facilitates adequate reduction of GdAc to $Gd(OH)_3$ and subsequent removal of the undesired water content. The Gd_2O_3 nanopowder has been acquired after calcination at a relatively high temperature (~600 $^{\circ}C$) for a time duration of nearly 5 h. Next, the product was subjected to repeated washing and centrifugation (~6000 rpm) followed by filtration steps prior to oven heating (~80 $^{\circ}C$) overnight. The process can be conceptualized as shown in **FIGURE.2.1** The final product i.e. undoped Gd_2O_3 nanopowder (GNP), is preserved in a desiccator for subsequent experimentation.

2.1.2. Processing of Gd_2O_3 nanophosphors via hydrothermal route

Knowing that top-down approach cannot deliver the requisite form of nanometric Gd_2O_3 from its bulk counterpart (being thermally and mechanically stable), an alternative strategy is adopted to suit the desired purpose [2, 3]. It involves a three-step hydrothermal process: (i) acidification, (ii) formation of hydroxide, and

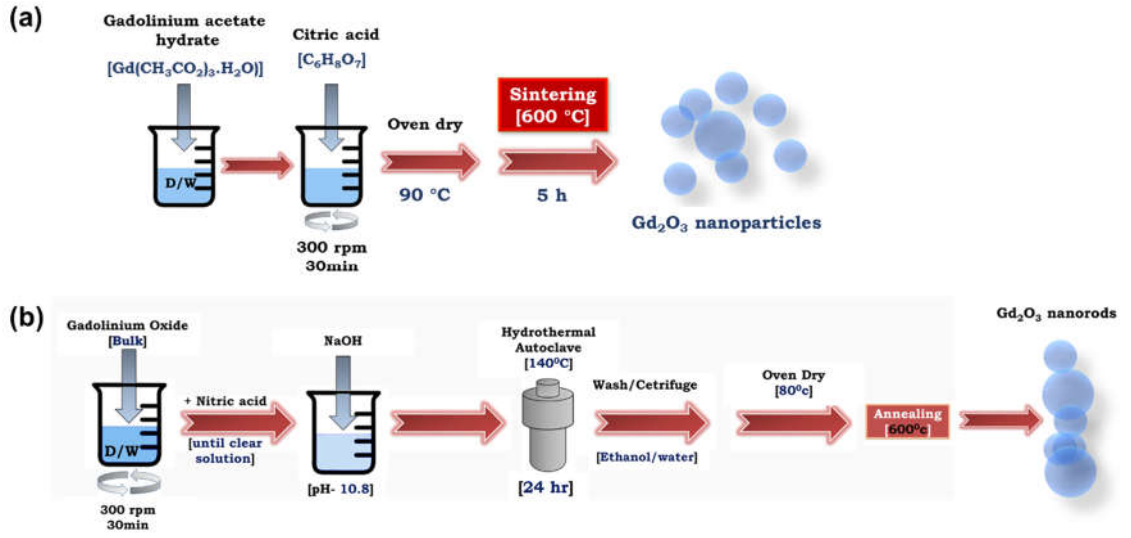

FIGURE 2.1. Schematic diagram of synthesis steps for preparing Gd_2O_3 based nanosystem following (a) citrate gel route and (b) hydrothermal route.

eventually (iii) reduction to its oxide form. At first, in an aqueous solution containing 0.5 g of bulk Gd_2O_3 and a suitable amount of conc. HNO_3 (69%) is added gently to obtain a nitrate product ($Gd(NO_3)_3$) in the form of a clear sol. In the next step, the addition of NaOH is considered so as to reduce the nitrate compound to a hydroxide product ($Gd(OH)_3$). In the next step, the precursor is subjected to autoclaving at a temperature of 140 °C in a polypropylene-lined autoclave, for a time duration of ~24 h. The final step involved calcination at a temperature of 600 °C, for a time duration of ~5 h.

2.2. Inclusion of Eu^{3+} as dopant and Na^+, K^+ as co-dopants.

In order to synthesize Eu^{3+} doped Gd_2O_3 nanopowder, suitable steps are followed considering key-reactants. A suitable amount of the reactant, Europium acetate (EuAc: $(CH_3COO)_3Eu$, CDH, 99.99% pure), is added to the solution after the completion of first step in the citrate gel route and consequently, several batches of nanoscale Gd_2O_3 systems are derived, with the inclusion of Eu dopant between, 1-7 mol%. The as-synthesized pristine and Eu-doped Gd_2O_3 nanosystems are marked as, GNP and EuGNP; respectively. Subsequently, 1 mol% Eu^{3+}:Gd_2O_3 (1% EuGNP), 3 mol% Eu:Gd_2O_3 (3% EuGNP), 5 mol% Eu:Gd_2O_3 (5% EuGNP), and 7

mol% Eu:Gd_2O_3 (7% EuGNP) are obtained and carefully preserved in a desiccator for further investigation.

In addition, doping of Eu^{3+} is also realized following hydrothermal method, where in stoichiometric amount (1 mol%) of bulk Eu_2O_3 powder (CDH, 99.99% pure) is added to the mixture in along with Gd_2O_3 bulk powder. Incorporation of Eu^{3+} into the Gd_2O_3 host as dopants was marked as 1% EuGNR.

Inclusion of alkali co-dopants into the host matrix is facilitated by both citrate gel route and hydrothermal route, by addition of suitable precursors. In case of citrate gel route, precursors used were sodium acetate (CH_3COONa, CDH, 99.99% pure) and potassium acetate (CH_3COOK, CDH, 99.99% pure) in stoichiometric proportions with the intention of incorporation of co-dopants as desired into 1% EuGNP nanosystem. Accordingly, we obtained samples co-doped with Na^+ and K^+ and labelled as, EuGNP(Na), and EuGNP(K); respectively. As for co-doping in the hydrothermal route, $NaNO_3$ (CDH, 99.99% pure) and KNO_3 (CDH, 99.99% pure) have been selected and transferred separately to the concerned precursor. The respective samples obtained are labelled as, EuGNR(Na) and EuGNR(K).

It is important to mention that the amount of alkali precursors, i.e., alkali acetates and alkali nitrates employed were so chosen that the ionic ratio between dopant RE ions (Eu^{3+}) and alkali $(M)^+$ ions remains equal in the solution. For instance, in order to acquire equal ionic concentrations between the dopant and co-dopant, 5 mg of $(CH_3COO)_3Eu$, and 2.4 mg of CH_3COONa and 2.83 mg of CH_3COOK are weighed and mixed suitably for preparing Na^+ and K^+ co-doped EuGNP systems; respectively. In contrast, for hydrothermally derived GNR systems, 5 mg of Eu_2O_3, and 2 mg of $NaNO_3$ (or 2.4 mg KNO_3) were added to fabricate Na^+ or K^+ co-doped EuGNR systems; respectively. The similarity in size and chemical behavior between the Eu^{3+} and Gd^{3+} ions would favor thermodynamically to yield the formation of RE compound readily. The requirement of an equal ionic concentration of Eu^{3+} and M^+ is crucial to support the accurate co-doping of the later within the system of interest.

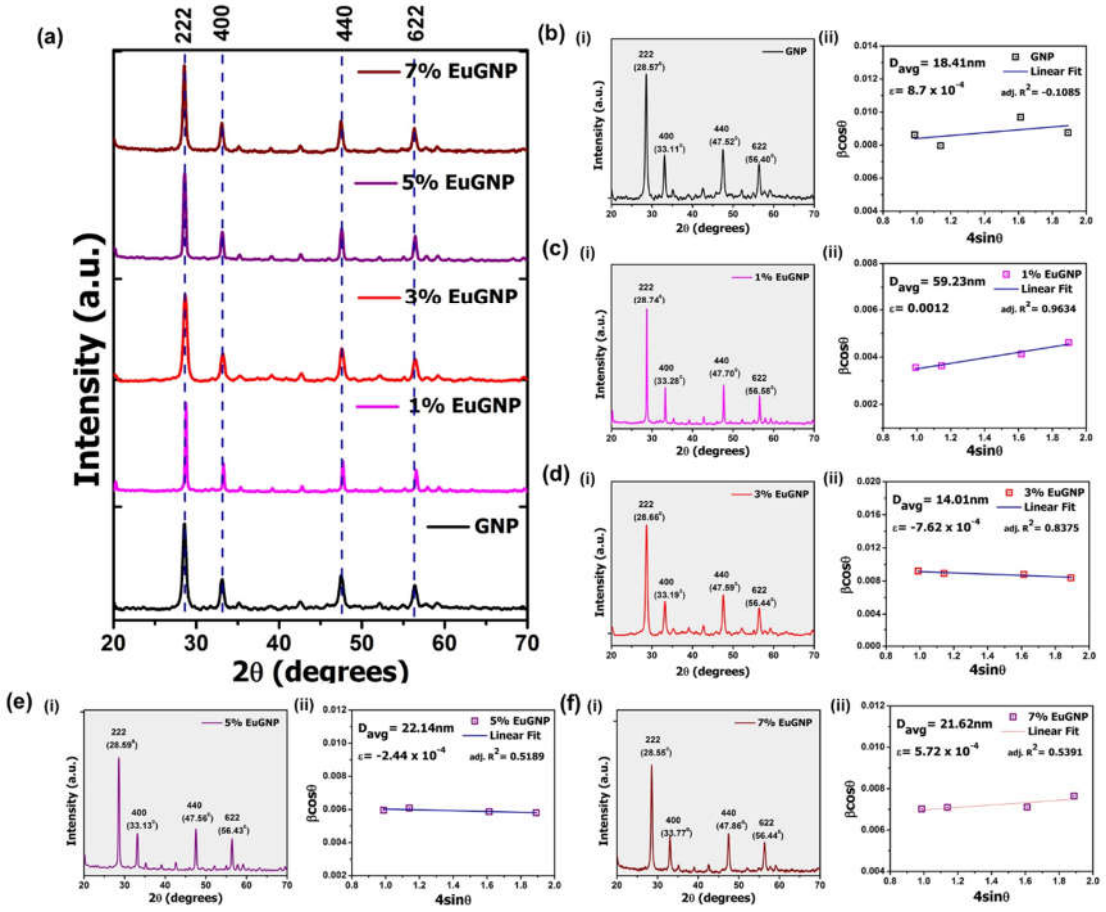

FIGURE 2.2. (a) Comparative plot for X-ray diffractograms of undoped and Eu^{3+} doped Gd_2O_3 nanosystems; (b-f) displays the difrractograms for individual samples along with the Williamson-Hall plots.

The nanoscale GNP and GNR products obtained are subjected to washing thoroughly and repetitively with the deionized (DI) water and AR-grade ethanol to make the derived systems free from any undesired species and subsequently, kept ready for further characterizations.

2.3. Basic characterization Gd_2O_3 nanoparticles (GNP) and Gd_2O_3 nanorods (GNR)

2.3.1 XRD analysis

A series of X-ray diffractograms of the undoped and Eu^{3+} doped Gd_2O_3 nanosystems are depicted in **FIGURE. 2.2 (a**), and then shown independently in **FIGURE. 2.2** (b-f).

TABLE 2.1. XRD peak positions, FWHM values and the determined average crystallite sizes for as-prepared GNP and EuGNP nanosystems

Plane	GNP			1% EuGNP			3% EuGNP			5% EuGNP			7% EuGNP		
	Center (°)	FWHM (°)	D_{avg} (nm)	Center (°)	FWHM (°)	D_{avg} (nm)	Center (°)	FWHM (°)	D_{avg} (nm)	Center (°)	FWHM (°)	D_{avg} (nm)	Center (°)	FWHM (°)	D_{avg} (nm)
[222]	28.56	0.52	**18.41** ± 0.85	28.74	0.21	**59.23** ± 1.24	28.65	0.56	**14.01** ± 0.42	28.59	0.36	**22.14** ± 0.89	28.55	0.43	**21.62** ± 0.74
[400]	33.10	0.49		33.28	0.22		33.19	0.55		33.12	0.37		33.07	0.44	
[440]	47.51	0.62		47.70	0.27		47.59	0.57		47.55	0.38		47.48	0.46	
[622]	56.39	0.58		56.57	0.31		56.44	0.56		56.43	0.39		56.34	0.51	

The diffractograms essentially show four prominent peaks positioned at the respective Bragg angles (2θ) of 28.57°, 33.11°, 47.52°, and 56.4° and assigned to the (222), (400), (440), and (622) crystallographic planes of the cubic phase Gd_2O_3 system, with space group no. 199 (I-2_1 3) (JCPDS no. 76-0155) [4].

We employed Vesta® to determine the interplanar spacings of the afore-mentioned crystallographic planes and found to be, ~0.31 nm, 0.27 nm, 0.19 nm and 0.16 nm. Ignoring the instrument line broadening aspect, the average crystallite size (d) and micro-strain (ϵ) of the nanosystems can be estimated th rough the well-known Williamson-Hall (W-H) formula:

$$\beta cos\theta = \frac{0.9\lambda}{d} + 4\epsilon\, sin\theta \qquad (1)$$

In Eqn. (1), β is the full width at half maxima (FWHM) in radians, θ is the diffraction angle in degrees and λ is the wavelength (1.543 Å) of the X-rays employed. We obtained d ~18 nm for GNP, while typical microstrain value is of the order of 10^{-4}, for most cases. The corresponding peak positions, FWHM values and the determined crystallite sizes for all the as prepared GNP nanosystems are depicted in **Table 2.1.**

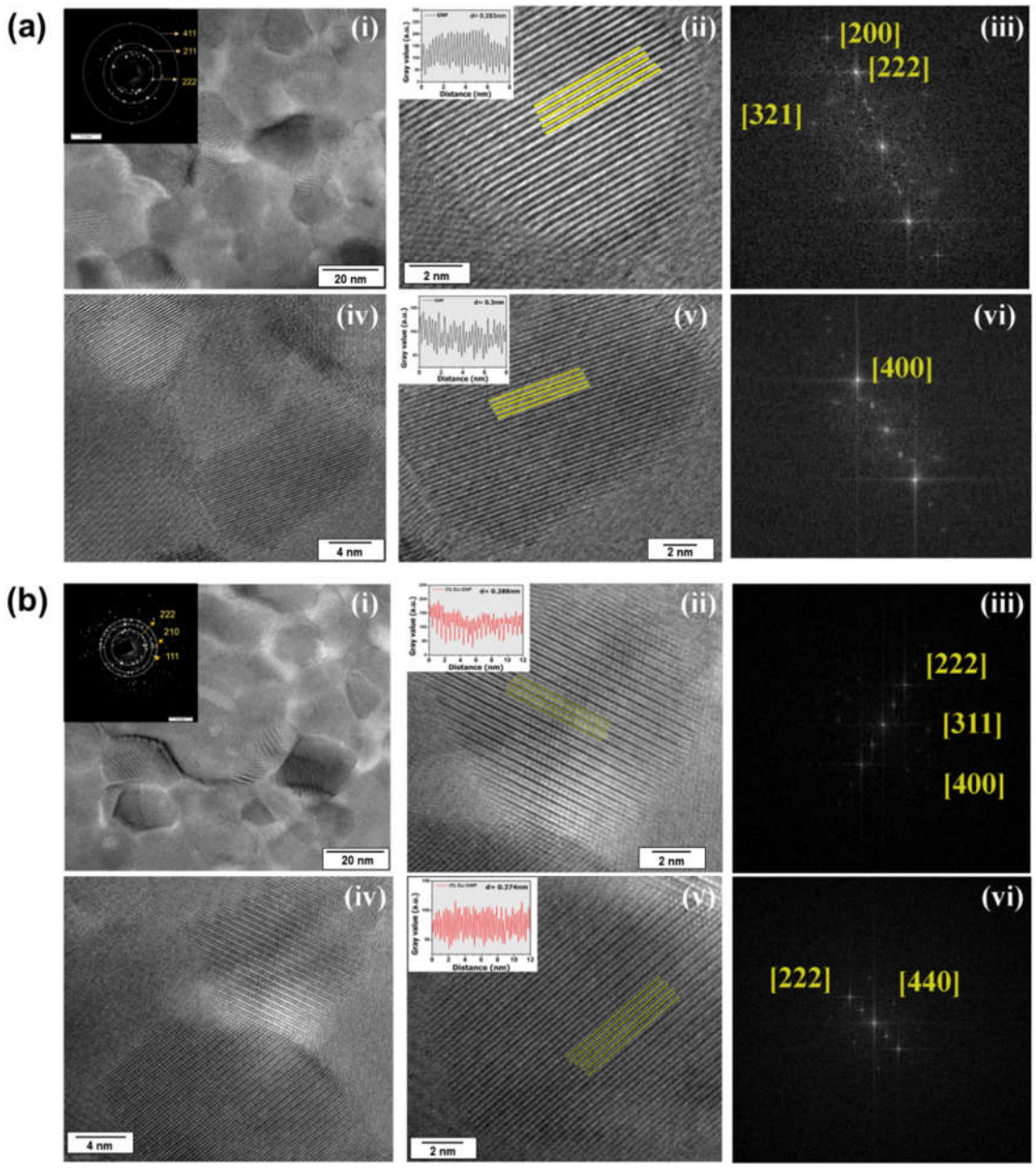

FIGURE 2.3. TEM images for (a) GNP and (b) 3% EuGNP with the respective SAED patterns as insets in (i). Magnified portions of (i) displaying fringe patterns are shown in (ii), (iv) and (v). The insets in (ii) and (v) are plots for gray scale vs distance to signify the lattice spacing feature. The FFT of images (ii) and (v) are shown in (iii) and (vi). The analysis and calculations were made using *ImageJ®*.

2.3.2 Morphological analysis

The microscopic information can be visualized through the TEM images, depicted in **FIGURE 2.3 (a,b).** Here, nanocrystalline feature of the GNP and 3%EuGNP

specimens with a very thin amorphous surface layer due to citric acid coating has been witnessed. The SAED patterns, shown as figure-insets in sub-figure **(i)** essentially exhibit concentric ring-type patterns along with distinct bright spots featuring local departure from the perfect periodicity. In both **FIGURE 2.3 (a)** and **(b),** shown in (iv), the magnified part of (i), would highlight nanoparticles with lattice fringes oriented in different directions. In **FIGURE 2.3 (a),** the HRTEM sub-figures (ii) and (v) represent lattice fringe patterns of two distinct nanoparticles highlighting positions of the normal atomic sites and point defects. With the help of *ImageJ*®, the respective interplanar spacings were determined from the plots for grey values against distance and estimated to be, ~0.28 nm and ~0.3 nm and corroborate with the (400) and (222) planes of the cubic phase Gd_2O_3; respectively [5]. Corresponding fast Fourier transform (FFT) images of the two-lattice pattern-types are shown in (iii) and (vi). Similar analyses were also made for 3% EuGNP specimen with corresponding lattice spacings' being ~0.27 nm and 0.29 nm for (400) and (200) planes; respectively.

2.3.3 Optical band gap determination

The absorption and reflectance characteristics of the GNP and EuGNP nanosystems can be found in **FIGURE 2.4**. As for the undoped GNP system (**FIGURE 2.4 (a)),** a poorly resolved peak observed at ~230 nm arises due to the $^8S_{7/2}$ to $^6D_{9/2}$ transitions within the Gd^{3+} matrix and otherwise termed as host excitation band by earlier groups [6]. In case of 1% and 3% doped EuGNP nanosystems, the broad peak maxima at ~276 nm, 360 nm have arisen due to intra *f* band transitions of Eu^{3+} ions. However, these *f-f* transitions are absent in case of 5% and 7% EuGNP nanosystems (**FIGURE 2.4 (d, e)).** Instead, a 'charge transfer band' (CTB) centred ~235 nm and arising due to the charge transfer between the 7*f* orbitals of the dopant Eu^{3+} and 2*p* orbital of the host O^{2-} can be witnessed.

Usually, the optical band gap is derived from the Tauc's plot following the power law expression given by equation 2 below. Also, the optical band gaps can be determined through models proposed by V. Kumar *et. al*. [7]. Following eqn. 2,

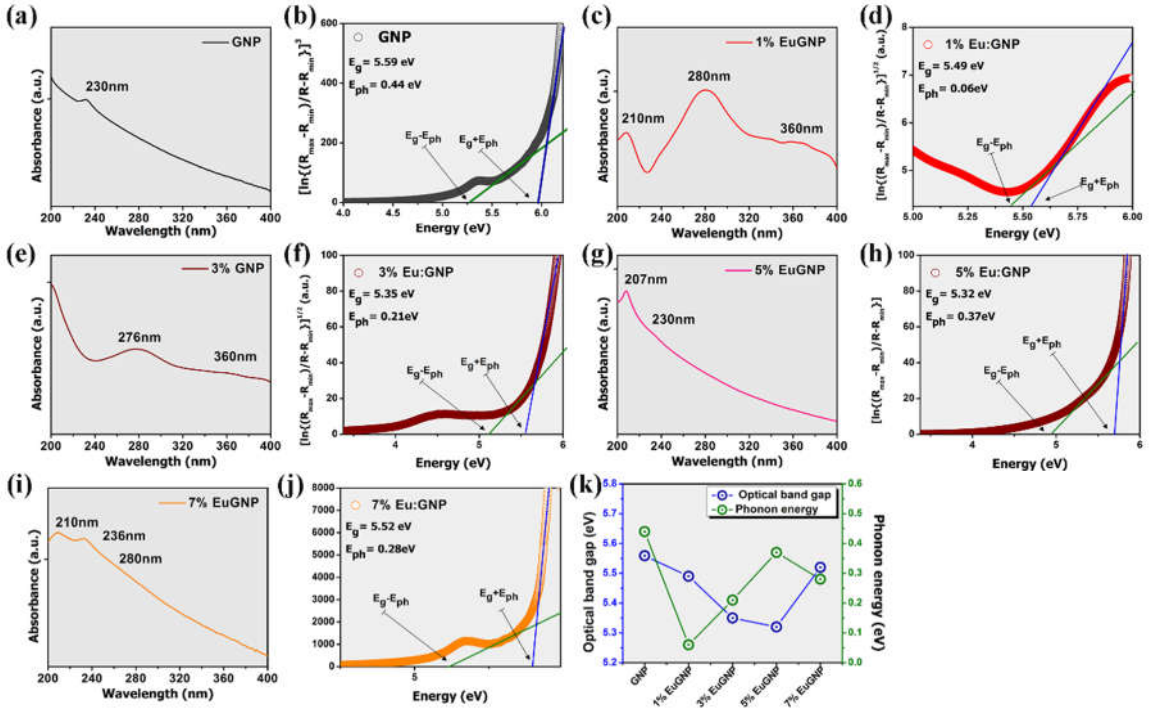

FIGURE 2.4. UV-Vis absorbance profiles (a, c, e, g, i) along with the optical band gap measured by Kumar's model in (b, d, f, g, h, i, j) of GNP , 1% EuGNP, 3% EuGNP, 5% EuGNP, 7% EuGNP respectively. (k) displays the comparative plot for the optical band gap and phonon energy determined for the various samples.

this method incorporates the phononic absorption and takes into account its contribution to the band gap as shown in **FIGURE 2.4** (b,d,f,h,j). We have,

$$\alpha(h\upsilon) = F(h\upsilon) = \frac{\{1 - R(h\upsilon)\}^2}{2R(h\upsilon)} \qquad (2)$$

$$\alpha h\upsilon = \frac{ln\left[\frac{(R_{max} - R_{min})}{(R(h\upsilon) - R_{min}}\right]}{2l} \qquad (3)$$

Here, 'α' is absorption coefficient, 'R' is reflectance, and 'l' as optical path length. While it is well known that Gd based oxides always characterize very wide band gap (~5 eV), in the present case it was estimated as, ~5.3 eV. The band gaps and phonon absorption energies for the undoped GNP and EuGNP systems, as predicted through Kumar's model are depicted in **FIGURE 2.4 (k) .** The plots for

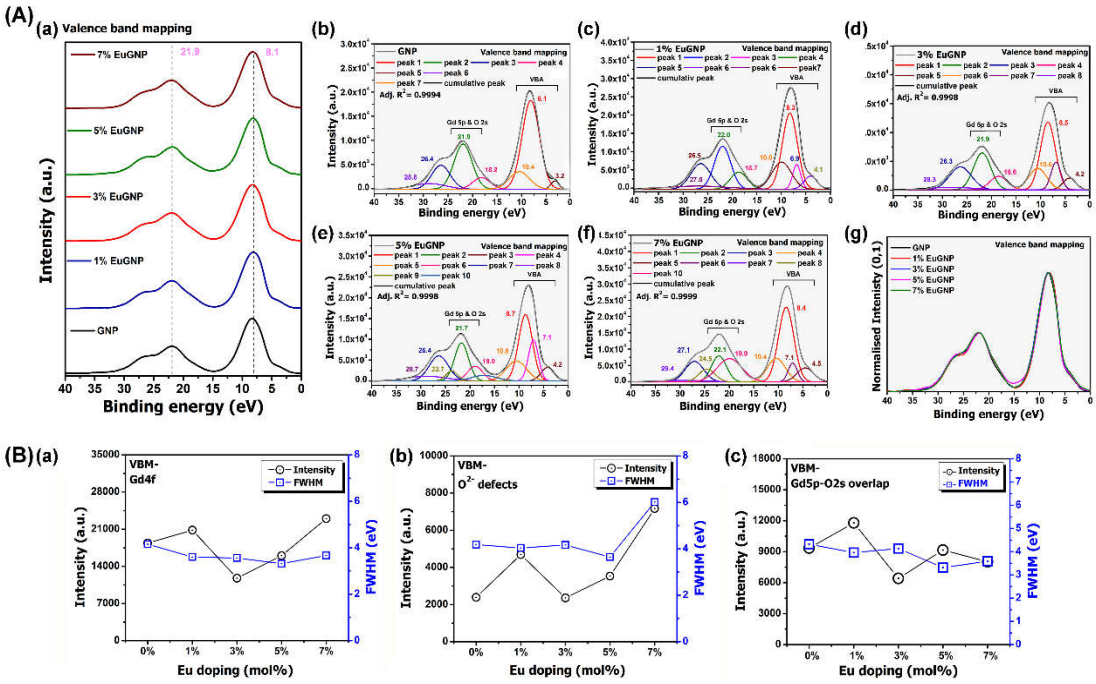

Figure 2.5. A(a) Comparative plot for valence band mapping (VBM) spectra of the as-prepared samples with individual deconvoluted profles shown in (b), (c), (d), (e) and (f) for GNP, 1% EuGNP, 3% EuGNP, 5% EuGNP and 7% EuGNP respectively; (g) displays the plot with normalized intensity for the above mentioned sample profles. **(B)** Comparative accounts of intensity of signals corresponding to (a) Gd4*f*, (b) O^{2-} defects, and (c) Gd5*p*-O2*s* overlap are shown.

Kumar's model feature two separate coordinates in the energy axis such that the gap between the points imply the gap between valence band maximum and conduction band minimum, i.e. the energy band gap E_g [8] . One of the co-ordinate corresponds to the value of 'E_g+ E_{Ph}', while the other corresponds to 'E_g - E_{Ph}' where 'E_{Ph}' is phonon energy participating in the optical transition [9]. We conclude that absorption edge of the prepared nanosystems are formed by the phonon-assisted optical transitions.

2.3.4 XPS based revelations

2.3.4.1 Valence band mapping

XPS valence band spectra corresponds to the interpretation of occupied density of states in a material, analysing loosely packed electrons which are directly involved in the bonds between atoms and contribute to the valence band structure of the system [10]. The valence band mapping (VBM) spectra of the prepared samples can be found in **FIGURE 2.5 (A) (a).** Upon appropriate deconvolution with the background according to the well-known Tougaard's rule they are depicted in **FIGURE 2.5 (A) (b-f)** [11]. The most important observation in the spectra, i.e. the valance band maximum is determined to be ~8.4 eV, which is typical for cubic Gd_2O_3 phase [12]. The plot with normalized intensity in **FIGURE. 2.5** (**A) (g)** reveals that the spectra for all europium doping levels retain their profile.

In order to have a better insight into the valence band structure and influence of Eu incorporation, we determined the intensity and FWHM ratios as shown in **FIGURE 2.5** (B), involving the various states. In **FIGURE 2.5** (B) (a), we observe an intensity drop for Gd*4f* in 3% doped system with a rise in higher doping levels; similar observations are also made for Gd*5p*-O*2s* overlap. In **FIGURE. 2.5** (B) (b), we observe a maximal peak intensity for the signal corresponding to O^{2-} defects in the case of highest doping level considered- i.e., 7% doped EuGNP system. We also observed that, the intensity ratio for Gd*4f* and the Gd*5p*-O*2s* overlap is maximum for such case (**FIGURE 2.5** (**B) (c)**).

2.3.4.2 XPS based surface revelations

Figure 2.6 (A) (a-e) displays the complete XPS spectra revealing Gd*4d* and *3d* states along with the occurrence of O*1s* peak. Upon Eu inclusion as dopant, a short peak ~1137 eV has been observed, which is of prime interest as this peak is a characteristic of 3+ oxidation sate of Eu [13]. Auger lines are prominent in any spectrum and are also observed in *K-L-L* shells ~ 1013, 999, 978 eV etc. Moreover,

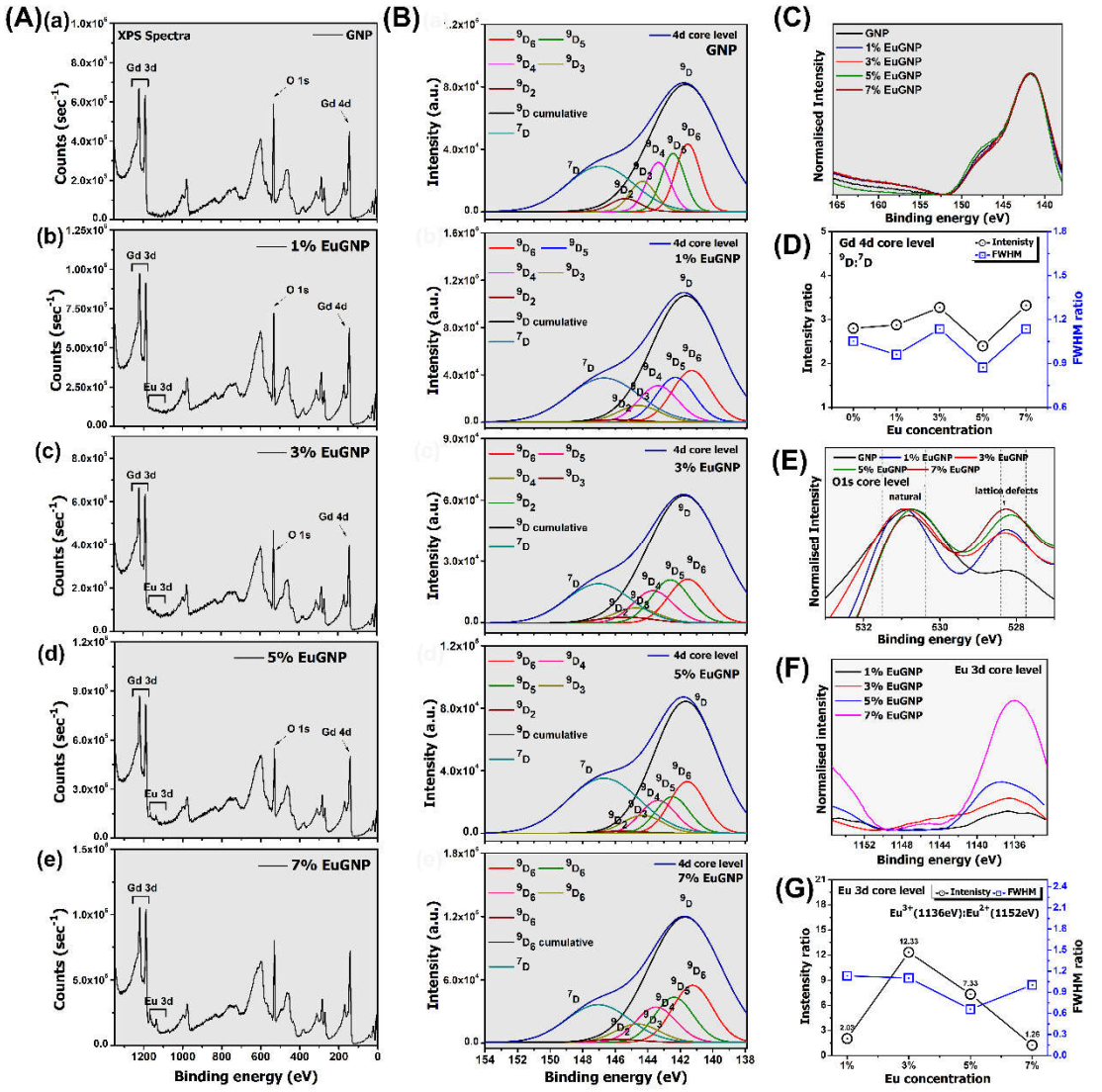

FIGURE 2.6.A(a-e) displays the complete XPS spectra revealing Gd *4d* and *3d* states along with occurrence of O*1s* peak. XPS core level spectra corresponding to the Gd*4d* photoemission lines observed were studied comprehensively, as shown in (C) with their deconvoluted profiles in B(a-e) for the various dopant concentrations respectively. (D) exhibits Intensity ratio as well as FWHM ratio of ^9D state (~147 eV) with respect to ^7D state (~143eV) in Gd*4f* profiles while (E) displays the core level spectra for O*1s*. (F) shows the Eu^{3+} 3d core level spectra for the rare earth samples with plot for intensity and FWHM ratio for prominent peaks observed are shown in (G).

we captured peaks at ~529.8 eV, corresponding to the known 3+ oxidation state of Gd [14]. All dopant concentrations, except the upper limit (7%EuGNP) case, have offered the aforesaid peak.

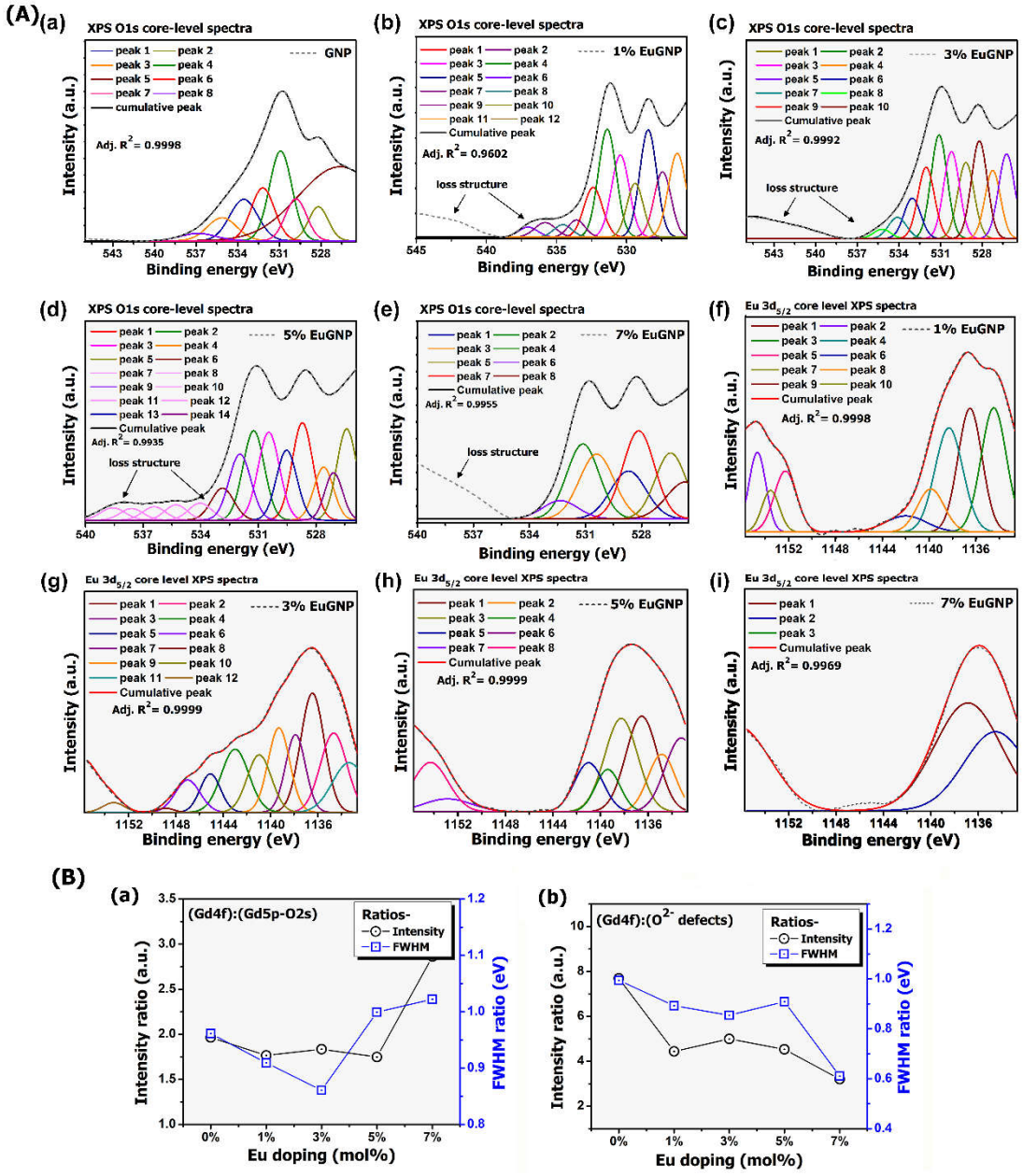

FIGURE 2.7. A) De-convoluted O1s core level (a-e) and Eu3d core level XPS spectra (f-i) for GNP, 1% EuGNP, 3% EuGNP, 5% EuGNP and 7% EuGNP respectively. (B) Intensity ratios of XPS core level spectra for Gd4f with respect to (a) Gd5p-O2s (b) O^{2-} defects.

2.3.4.3 XPS Gd*4d* and O*1s* Core level spectra (CLS)

The XPS core level spectra, corresponding to the Gd*4d* photoemission lines observed are exhibited comprehensively (**FIGURE 2.6** (C)). Shirley rule for background correction was followed while deconvolution and two major peaks were displayed in **FIGURE 2.6 (B) (g-k)** [15]. The peak maxima ~142 eV is

Table 2.2 Signals observed and accordingly assigned for XPS *O1s* core level spectra for undoped and Eu^{3+} doped Gd_2O_3 nanosystems

XPS core level spectra	Excess O and lattice defects			Natural lattice oxygen			Gd-OH bond			Anamolous bond		
	Center (eV)	Intensity ratio	FWHM	Centre (eV)	Intensity ratio	FWHM	Center (eV)	Intensity ratio	FWHM	Center (eV)	Intensity ratio	FWHM
GNP	528.2	-	1.7	532.2	ref	2.0	533.6	ref	2.4	535.1	ref	2.5
				530.9	1.7	1.9						
				529.8	0.8	1.8						
1% EuGNP	528.5	2.1	1.4	531.4	1.4	1.5	533.6	0.3	1.4	535.8	0.4	1.7
				530.4	1.0	1.5	532.4	0.8	1.6	534.5	0.4	1.5
				529.4	0.7	1.4						
3% EuGNP	528.2	1.3	1.4	532.0	0.6	1.4	534.1	0.2	1.5	536.1	0.1	1.2
				531.1	0.9	1.4						
				530.2	0.8	1.3						
				529.2	0.7	1.4	533.0	0.5	1.4	535.2	0.2	1.4
5% EuGNP	528.7	1.5	1.3	532.9	0.3	1.4	534.0	0.2	1.4	536.4	0.3	1.4
				532.0	0.7	1.3						
	528.1	0.8	1.2	531.2	0.9	1.3						
				530.5	0.9	1.3						
				529.5	0.7	1.3						
7% EuGNP	528.1	2.1	2.0	532.3	0.3	2.2	--------	--------	---------	---------	---------	---------
				531.1	1.1	2.0						
				530.4	1.0	2.2						

assigned to the Gd(III) species, while the other peak at 147 eV can be considered mainly due to low-spin of the system, with a usual spin polarization of 0.39 [13].

In **FIGURE 2.6 (D)** we find both the Intensity ratio as well as FWHM ratio of ^9D state (~147 eV) with respect to ^7D state (~143 eV). Whereas, **FIGURE 2.6 (E)** displays the core level spectra for O*1s* of the various samples characterizing a plot profile with asymmetrical twin peaks between 535 eV and 530 eV. O1s spectra typically consists of a main signal due to O^{2-} and Gd^{3+} bond at ~529.4 eV, while the sub-peak located at 532.1 eV is due to the hydrated oxygen species [31]. The deconvoluted spectra **FIGURE. 2.7 (a-e))** reveals a rather very complex nature of overlapping peaks, assigned to the contributing factors as mentioned in **Table 2.2.**

2.3.4.4 XPS Eu*3d* Core level spectra

FIGURE 2.6 (F) essentially depicts the Eu*3d* CLS for the EuGNP samples in which the spectra gained a well-defined profile as the doping concentration tends to increase. The major peaks of our concern could be probed after deconvolution, first being centred at, ~1136 eV while other one appeared as satellite peak at, ~1152 eV that corresponded to 3+ and 2+ oxidation states of Eu, respectively [16-18]. The

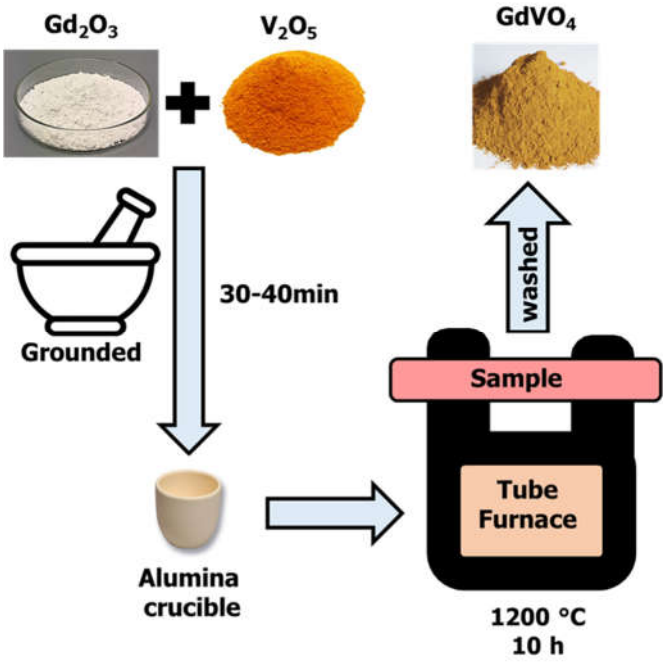

FIGURE 2.8 Schematic flow diagram for synthesis route of $GdVO_4$ nanosystem via (a) solid state reaction

deconvoluted spectra are presented in **FIGURE. 2.7** (f-i)), while **FIGURE 2.6** (G) displays the plot for intensity and FWHM ratio of the concerned peaks.

2.4 Solid-state derived $GdVO_4$ nanosystem and Eu^{3+} doping

To obtain nanoscale $GdVO_4$ powder, a simple and facile two step solid state synthesis route has been adopted. Reports do exist in literature detailing preparation of RE-vanadate system following the solid-state reaction **[19-21].** To elaborate the procedure, firstly bulk gadolinium oxide (Gd_2O_3, CDH, ~99.9% pure) is mixed with an equimolar content of vanadium pentoxide (V_2O_5, CDH, ~99% pure) and grounded homogeneously for 30 min. in a mortar. The finely grounded mixture was placed in an alumina crucible and subjected to a tube furnace for nearly, 10 h and at a temperature of 1200 ˚C **[20]**. The as-received sample collected at room temperature were washed several times with DI water and ethanol to yield the desired nanopowder product. In order to obtain the doped nanosystem, we introduced appropriate molar fractions of Eu_2O_3 during the grounding step only. Accordingly, we obtained the undoped $GdVO_4$ (GdV),

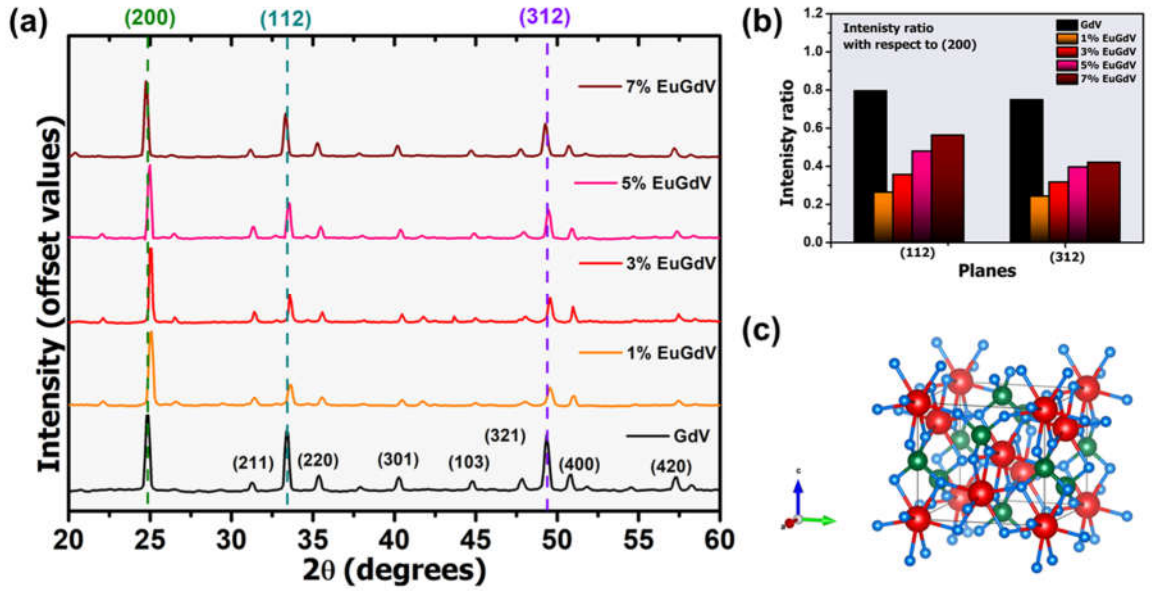

FIGURE 2.9 (a) Comparative XRD patterns for as-prepared nanosystems in the range of Bragg angle 20-60^0. (b) Relative intensity of the (112) and (312) peaks as compared with respect to intensity of most intense (200) peak. (c) Illustrative ball and stick figure symbolizing crystal structure of tetragonal GdVO4 with *s.g.* I-4_1/amd and axial ratio ~ 0.87 Å, obtained using Vesta®. The red, green and blue balls denote Gd, V and O atoms respectively.

and 1%, 3%, 5% and 7% Eu^{3+} doped $GdVO_4$ (EuGdV) nanosystems were from the reaction mixture. The entire method of preparation can be visualized following the scheme shown in **FIGURE 2.8**. As yielded products were washed thoroughly and kept ready for further characterizations.

2.5 Basic characterization $GdVO_4$ nanoparticles (GdV) and $GdVO_4$:Eu^{3+} (EuGdV) nanosystems

2.5.1 XRD analysis

The XRD patterns of as-prepared $GdVO_4$ samples are shown in **FIGURE. 2.9** (a) which essentially characterize the tetragonal zircon-type crystal structure, with space group I $4_1/amd$ (JCPDS 86-0996) **[22-25].** Earlier, $REVO_4$ was reported to crystallize in two different phases: zircon and monazite- types **[24].** Among these, zircon ($ZrSiO_4$)-type tetragonal crystal system is the most studied crystal phase where the RE^{3+} ions occupy single coordination environment with D_{2d} symmetry

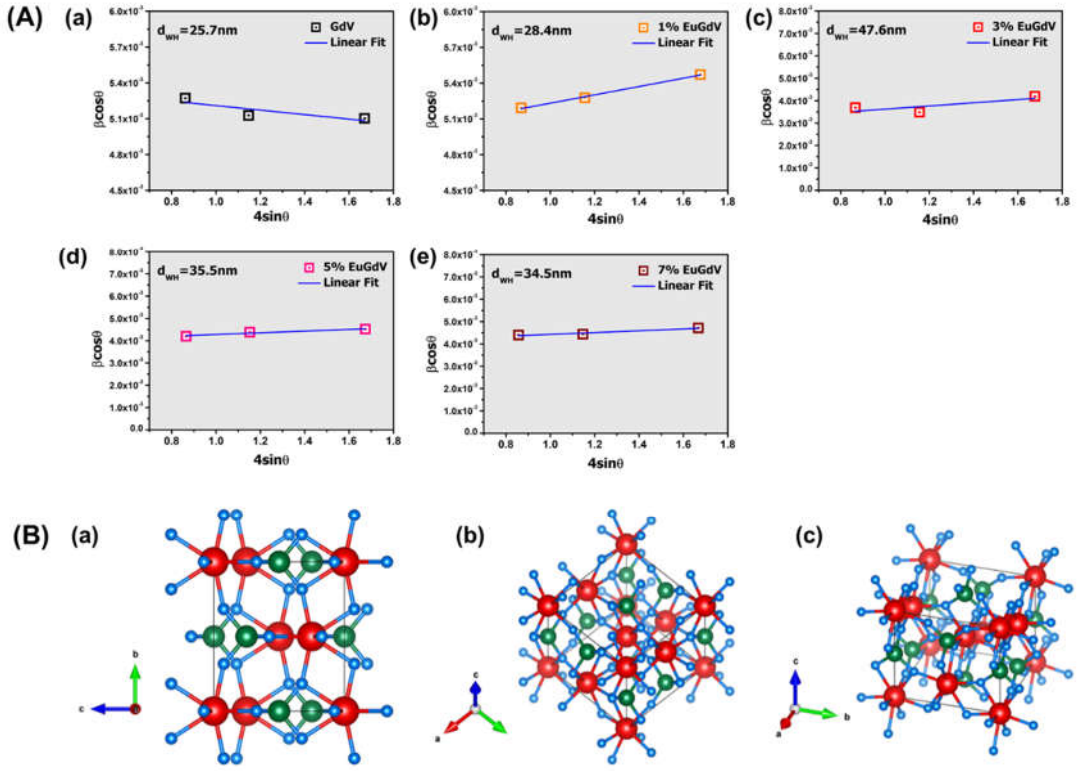

FIGURE 2.10 (A) Williamson Hall plots for (a) GdV, (b) 1% EuGdV, (c) 3% EuGdV, (d) 5% EuGdV and (e) 1% EuGdV. (B) Schematic illustrations of crystal structure obtained using Vesta® oriented along the projection and upward vector (a) [200] (b) [112] and (c) [312].

[26, 27]. Whereas, the monazite ($CePO_4$)-type monoclinic structure (e.g., *P21/n*) is rarely discussed in literature **[27, 28].** The diffractograms of 1%, 3%, 5% and 7% EuGdV also offer similar patterns with varied intensity but without introduction of any extra phase indicating high crystallinity of the products (**FIGURE 2.9(a)**). The lattice constants are calculated to be a=7.18 Å and c=6.31 Å, and the estimated axial ratio (c/a) is 0.87 corresponding to that of pure tetragonal $GdVO_4$ **[17].**

The average crystallite size 'd_{DS}' is calculated using Scherrer formula (Eqn.4) and was found to be in the range ~25-38 nm.

$$d_{DS} = \frac{0.9\lambda}{\beta cos\theta} \qquad (4)$$

The estimated size is comparatively smaller than the reported sizes ~ 50-90 nm obtained at calcination temperature beyond ~900 ˚C and with dopant concentrations below 10% [29]. The microstrain and crystallite size are also calculated using popular Williamson-Hall plot for 'd_{WH}' as well (**FIGURE 2.10**), following Eqn. 1, mentioned in earlier sections.

In both the equations 1 and 4, 'β' is the FWHM in radians, 'θ' is the diffraction angle in degrees and 'λ' is the wavelength (1.543 Å) of the X-rays employed. Again, the crystallite sizes were determined to be in the range of 25-48 nm, similar to our observations made using Scherer's equation. The typical microstrain, 'ε' was found to be of the order of 10^{-4} in all the cases with a negative slope only in case of undoped GdV. A comparison as regards increment in the intensities of (112) and (312) peaks relative to (200) peak with increasing dopant level can be found in **FIGURE. 2.9** (b). Apparently, this implies a figurative effect of change in preferred orientation of crystallites upon inclusion of a dopant into the nanosystem. The representative crystal structure of $GdVO_4$ obtained through Vesta® is depicted in **FIGURE. 2.9 (c).** To have a better understanding of the crystal structure relevant to related orientations, the illustrations were refigured for the major projection and upward vector along the normal to [200], [112] and [312] and depicted in **FIGURE 2.10** (B) (a-c), as the case may be.

In fact, the orthovandate structure comprises VO_4 tetrahedrons and GdO_8 polyhedrons. It is the central V^{5+} ion which forms a tetrahedron VO_4 with the nearest four oxygen ligands such that the V–O with a bond distance of ~1.7 Å while the angles differ slightly from those of a regular tetrahedron (O–V–O are 108.19˚ and 110.18˚) [20, 30]. Meanwhile, the host Gd^{3+} forms a bis-disphenoid with eight nearest oxygen ligands, revealing two different bond lengths of Gd–O leading to a highly asymmetric environment on Gd^{3+} as such [20, 30]**.** In a regular Eu^{3+}:$GdVO_4$ lattice, dopant Eu^{3+} replaces host Gd^{3+} with a D_{2d} symmetry and occupies a 4a site of symmetry -4*m*2. The GdO_8 dodecahedra with VO_4 forms chains extended along the *c*- axis, while in the *ab* plane GdO_8 dodecahedra cages

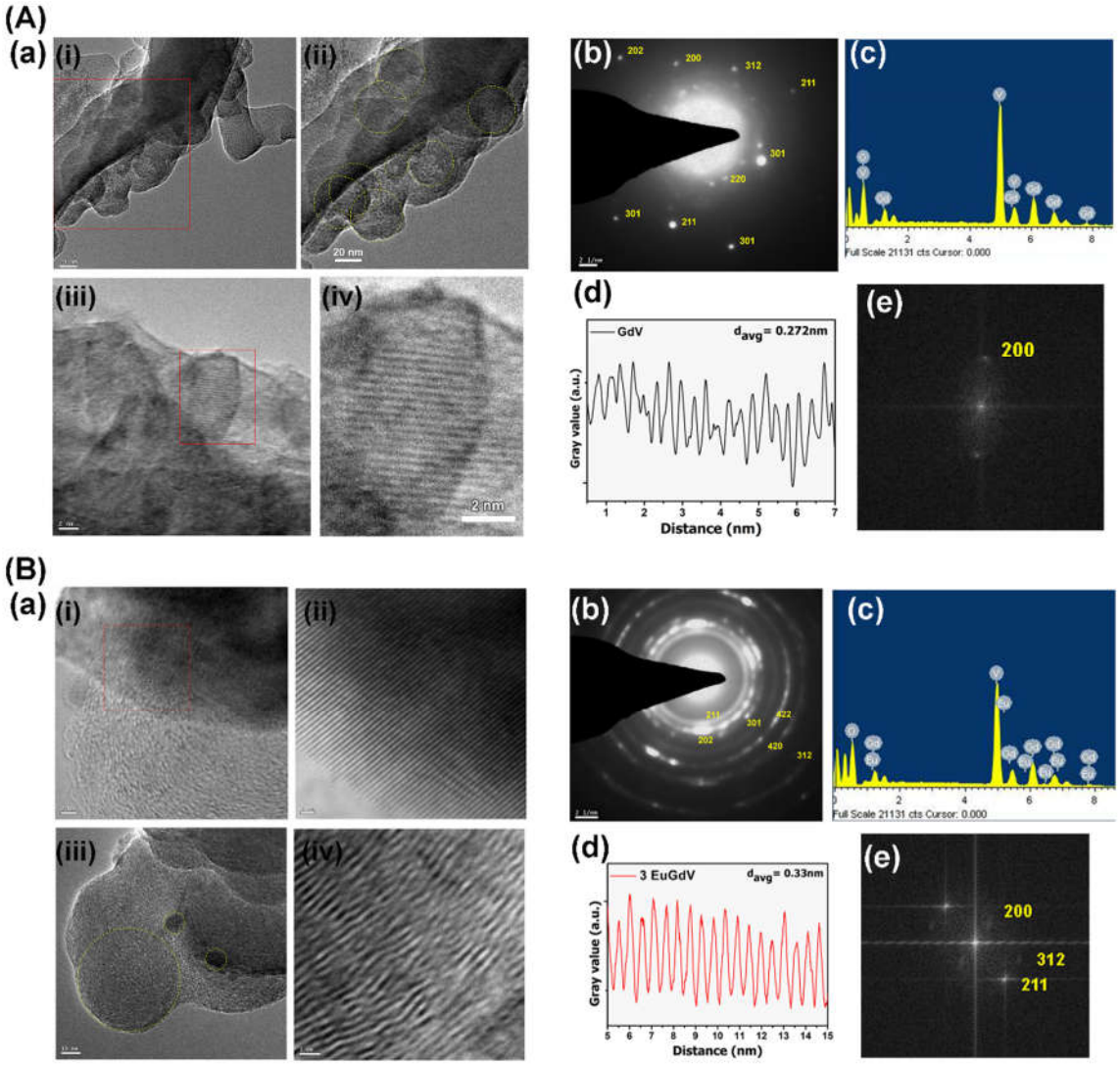

FIGURE 2.11 TEM images (a) (i-iv) for (A) GdV and (B) 3% EuGdV nanosystem. SAED pattern with characteristic spots observed is displayed in (d). EDX spectra is shown in (c). HR-TEM images revealing lattice fringe are shown in (a) (iv), with corresponding (d) plot profile and (e) Fast Fourier Transform of the same

are linked with four adjacent VO_4 at corners alternatingly such that two are positioned along [100], and the remaining along [010] directions [24]**.** The Gd–O bond distance depends on the type of oxygen to which the Gd^{3+} ion is attached *viz.*, 2.4 A˚ (corner) and 2.6 A˚ (edge) [31]. The absence of impurity phases and a very small shift of reflections compared to the reflection positions of pure $GdVO_4$ indicate that the dopant ions are adequately incorporated into the $GdVO_4$ host lattice.

2.5.2 Morphological analysis

Morphological studies of GdV and EuGdV were made using TEM imaging and shown in **FIGURE 2.11** (A) (a) (i-ii), which reveals clumps of nearly spherical $GdVO_4$ nanoparticles being present in a sheet-like base. Our observations are analogous to previous reports on microscopic imaging of solid state derived $GdVO_4$, which displays crystalline, polyhedral and slightly agglomerated bunches of smaller particles **[21, 23, 24, 32, 33]**. High sintering temperatures, beyond 1000 ˚C must be the chief reason behind agglomeration and clustering of smaller particles **[21]**. Figure 2.11 B (a) (i-ii) shows TEM images for 3% EuGdV which also indicate similar morphological feature as that for GdV case. The selected area electron diffraction patterns (SAED) are shown in Figure (A), (B)-(b), which revealed scattered bright spots around the diffused ring patterns in case of GdV and diffused, yet prominent rings in case of 3% EuGdV confirming substantial polycrystallinity. With an oriented crystallographic axis of the system, the planes responsible for the occurrence of the spots are designated suitably upon calculating the radius of the spots/rings using *Image J*®.

HR-TEM images revealing lattice fringes of the respective samples are Figure 2.11 (A), and (B), (a)(b), (iii-iv). The *d*- spacing are calculated from the plot profiles generated using *Image J*® displayed in **FIGURE 2.11** (A, B)- (d), and were determined to be 0.27 nm and 0.33 nm for GdV and 3% EuGdV; respectively. To be mentioned, these *d*-spacing belonging to the respective planes of (200) and (312), determined using *Vesta*® [JCPDS 86-0996], and designated in FFT images, shown in Figure 2.11 (A), (B), (a)(b)- (e). The indices observed are in good agreement with the planes outlined in the XRD analysis**.**

In the energy dispersive X-ray spectra (EDX) based elemental analysis of the specimens, characteristic signals arising from all expected constituents corresponding to different binding energies can be easily traced. **Figure 2.11 (A)(c),** illustrates the EDX spectrum of GdV system indicating presence of Gd, V and O; while introduction of newer signals for Eu can be realized in case of 3%

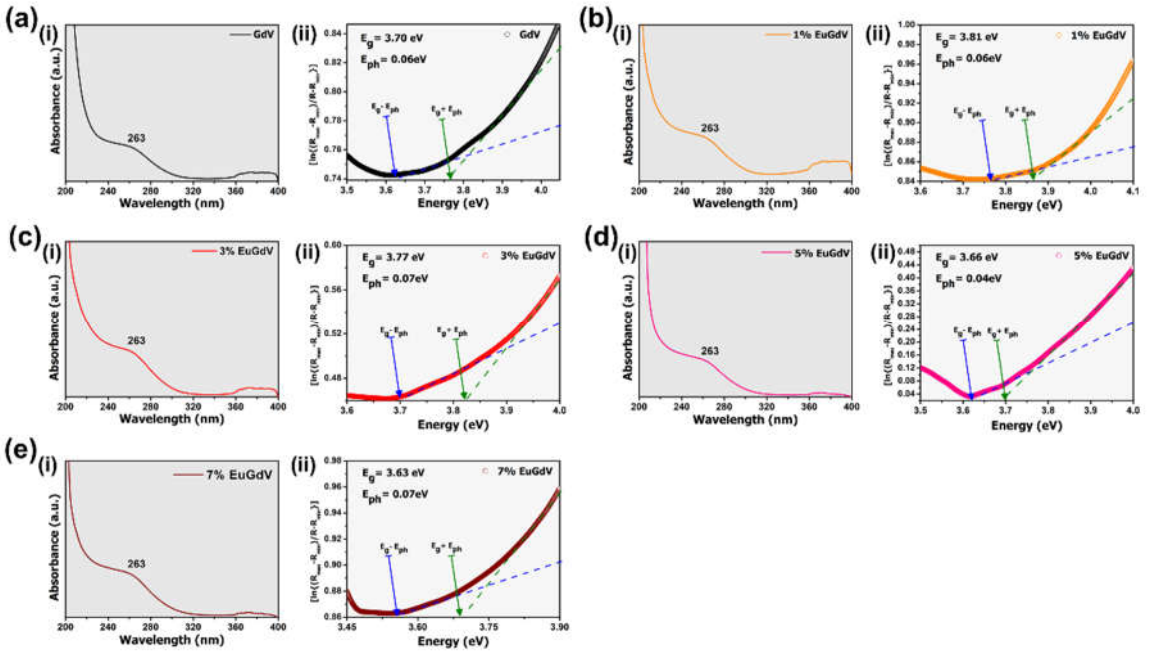

FIGURE 2.12. UV-Vis absorbance spectra of nanophosphors with optical band gap (calculated using Kubelka Munk method) shown as figure insets is shown in (i) for (a), (b), (c), (d), and (e) corresponding to GdV, 1% EuGdV, 3% EuGdV, 5% EuGdV, and 7% EuGdV respectively. Meanwhile the optical band gap and phononic energy calculated using Kumar's model are shown in (ii) for the above mentioned samples.

EuGdV case (**FIGURE 2.11 (B)(c)).** The distinct EDX line traces suggest that Eu^{3+} is incorporated into the host crystallites substantiating our discussion on the XRD based analysis.

2.5.3 Association of charge transfer bands and optical band gap determination

Like in any typical host sensitizing luminescent candidate, in Eu^{3+}:$GdVO_4$ absorption and consequently, energy transfer (ET) from the host to activators are hugely accountable for emission intensity and phosphor efficiency. Upon UV excitation, the energy absorbed through the $GdVO_4$ host is efficiently transferred to the Eu^{3+} centers. Figure 2.12 shows typical UV-Vis spectra in the UV region, which does not reveal any peak centering ~205 nm (corresponding to absorption by $4f^n$ of RE^{3+}), thereby implying effective energy transfer between VO_4^{3-} and $4f$ energy levels [34]. Intense broad bands ranging between 230-290 nm are accredited to charge transfer (CT) mediated transitions inside $[VO_4]^{3-}$ groups [21,

35]. It was proposed earlier that the CT assisted transition from $^1A_1$ to ($^1T_1$, $^1T_2$) would give rise to a doublet, broad structure as well as intense absorption band in the UV region wherein $^1A_1$ is the ground state and $^1T_1$, $^1T_2$ are excited states of VO_4^{3-}, in conformity with molecular orbital theory (MOT) [36-38]. Furthermore, one-electron CT also takes place between the O2*p* orbital and the vacant 3*d* orbital of the central vanadium (V^{5+}) in the tetrahedral VO_4^{3-} with T_d symmetry. The peak centered at ~ 263 nm can thus be attributed to the overlapping of two CT processes: (i) involving Eu–O (appearing at higher energy) and V–O components [39-41] and (ii) electric and dipole-allowed transitions from the $^1A_2$ to the ^1E and $^1A_1$ excited states of the VO_4^{3-} ion [25]**.** The weaker line at 396 nm is assigned to the *f –f* transitions of Eu^{3+}. The intrinsic Eu^{3+} absorbance at ~ 400 nm corresponding to general *f –f* transitions is much weaker than host excitation of the VO_4^{3-} groups, indicating that the excitation of Eu^{3+} is mainly through the VO_4^{3-} groups [42]**.**

Following Eu^{3+} in eight-coordination, the CT band (220 to 270 nm) overlaps with that of the vanadate group and a single broad peak is thus observed due to vanadate absorption followed by ET [19]. It is the CT transitions from the highest occupied molecular orbital (HOMO) level *i.e.* O^{2-} nonbonding orbitals, to the lowest unoccupied molecular orbital (LUMO) level composed of antibonding V3*d* orbitals and O2*p* orbitals, in tetrahedral VO_4^{3-}, which describe the origin of the intrinsic luminescence from RE-vanadates [43]. Earlier, optical band gap of RE-vanadate system has been reported to lie in range of ~3.28-3.75 eV [21]. Following Eqn. 2, we determined the optical band gaps to be 3.4-3.59 eV with several meV order increments upon increasing dopant concentration (1-7 mol%). Furthermore, the optical gaps are also estimated through a model proposed by V. Kumar *et.al*. [7]. As discussed earlier this band gap so determined (following Eqn. 3) incorporates the phononic absorption and takes into account its contribution to the optical transitions. The calculated values range, ~3.63-3.8 eV.

The difference in ionic radius of dopant and host ions can lead to moderate modifications of phonon density of states and can alter the observed energy band

gap [44]. This occurs due to involvement of an additional process in the transitions i.e. phonons emission component along with photon absorption [8, 9]. Furthermore, increment in band gap energies in vanadate nanosystem is, in general, ascribed to the Moss-Burstein (M-B) effect instead of quantum confinement, as the Bohr radii for vanadate hosts are quite small ~ 1.15 Å [45]. The effect describes a situation where the electron carrier concentration exceeds both the conduction band edge density of states and the Fermi level as well. As all the states below the Fermi level are occupied states, it would thus occupy a position in the conduction band itself. The small variation in the band gap can also be attributed to the presence of deep defect states for highly concentrated defect V^{5+} centers i.e. lower valence state. Oxygen vacancies and/or vanadium antisite defects/dislocations adjacent to Vanadium ion can induce numerous newer energy levels within the band gap allowing visible absorptions and consequently lowers the optical band gap **[46]**.

2.5.4 XPS based revelations

XPS analysis assists us to abridge surface revelations of nanomaterials with regard to oxidation states of the host and dopant ions present. As only limited number of reports are available concerning XPS studies of the RE-vanadate based nanosystem, here we plan to introduce valuable quantitative information emphasizing valence band mapping spectra of the Eu^{3+}:$GdVO_4$ nanosystem.

Following the identification of crystal structure of the as-prepared nanoscale sample and confirmation of presence of Eu as a dopant into the matrix, XPS survey was conducted to analyse the elemental oxidation states and to exploit the valence band mapping of the system. Figure 2.13 (i) signifies the XPS survey conducted on GdV and 3% EuGdV. The background for the XPS survey is corrected according to the well-known Tougaard rule [11]. The important revelations in the survey are signal determination of Gd4*d*, V2*p* and O1*s* orbitals. Peak centering at ~529.6 eV, agrees with the characteristic +3 oxidation state of Gd [14]. For 3% EuGdV, a weak peak at ~1137 eV has been witnessed, which is the

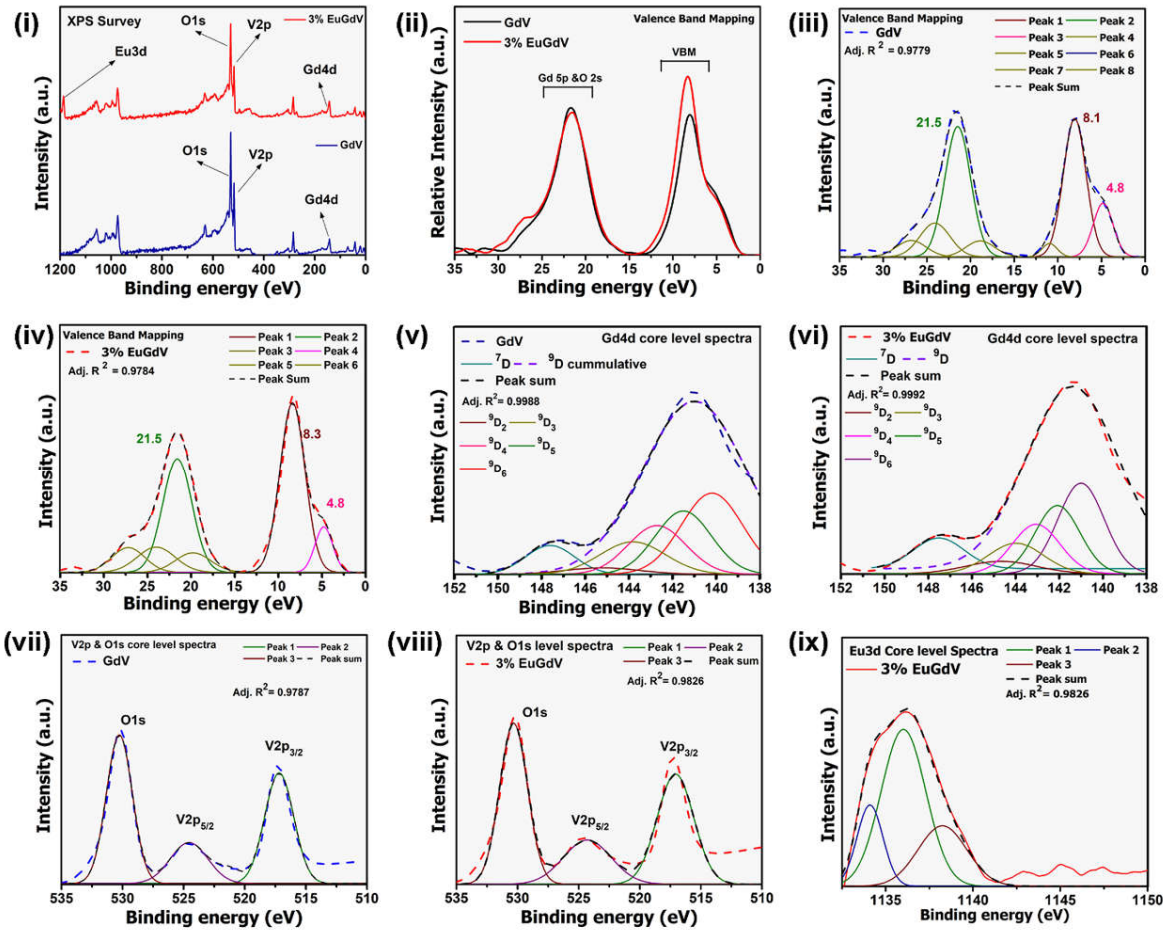

FIGURE 2.13: XPS survey of GdV and 3% EuGdV is shown in (i) with the comparative (ii) VBM displayed in (ii). The deconvoluted VBM is displayed in (iii) GdV and (iv) 3% EuGdV nanosytems. The CLS for the prepared samples for (v, vi) Gd4*d*, (vii, viii) V2*p* & O1*s* (ix) Eu3*d* respectively.

characteristic of +3 oxidation state of Eu offering added indication towards effective doping of Eu^{3+} in the $GdVO_4$ lattice [13, 47]. Not surprisingly, other prominent lines observed in the spectrum at 1013, 999, 978 eV etc. correspond to Auger lines.

Usually O2*p* partial states, Gd-O bonds, and Gd4*f* are determined in the range of 3-11 eV in the VBM spectra, as can be found in **FIGURE 2.13 (ii)** [12]. We observed that the valence band maximum is situated at ~8.06 eV [12]. The signal is attributed, in general, to Gd4*f* and interestingly upon 3% Eu inclusion, the VBM maximum is shifted to ~8.34 eV. It is noteworthy that in between ~17-20 eV, peaks due to O^{2-} (point defects) are observed, and in our case they are found to be very

weak. In the range of ~18-24 eV, however, the Gd5*p*-O2*s* overlap peak is apparently visible (at ~23 eV) [12]. We evaluated the intensity and FWHM ratios to obtain a fair assessment of the effect of Eu incorporation, involving the various states. The intensity ratio of signals for Gd4*f* and Gd*5p*-O2*s* overlap increased from ~1.1 for GdV to ~1.5 after introduction of Eu^{3+}.

It was known that the large electrostatic interactions between Gd4*d* (holes) and Gd4*f* (electrons) lead to a multifaceted multiplet structure for Gd4*d* core level spectra and can be observed in **FIGURE 2.13 (v, vi)** [12]. The plot displays a characteristic Gd4*d* doublet attributed to spin splitting by exchange interactions. The twin peaks were studied elaborately with a five-fold Voigt fitting and consequently, ^9D initial and ^7D final ionic states have been analyzed [48, 49]. The effect of dopant is seemingly minimal and thus suggests that incorporation of Eu^{3+} into the vanadate matrix does not interfere with the Gd4*d* states. A lower concentration of dopant ions in comparison to the most abundant host ones might be the sole reason behind such a situation.

In XPS spectrum of V2*p* as shown in Figure 2.13 (i), binding energy of V2$p_{3/2}$ and V2$p_{5/2}$ as positioned at 517.1 and 525 eV correspond to +5 oxidation state of V [50]. Upon deconvolution (**FIGURE 2.13 (vii, viii)**), we did not observe any multiplet splitting which is obvious as V^{+5} does not have any unpaired electrons [51]. A symmetrical peak fit suggests that V^{+5} has not undergone any decaying and other species viz. V^{+4}, V^{+3} etc. are absent in the nanosystem. Furthermore, the CLS reveals O*1s* peak at ~ 530.3 eV and are attributed to V-O and Gd-O bonds in tetragonal lattice of $GdVO_4$ [52]. As for the CLS signal for 3$d_{5/2}$ ~1136 eV (characteristic of Eu^{3+}) is realized, while no other signal for Eu^{2+} state can be found [53]. This observation further provides substantial evidence that the Eu^{3+} is doped into the vanadate system appropriately.

2.6 Concluding remarks

REO and $REVO_4$ nanosystems were prepared following diverse physicochemical routes including both bottom-up and top-down strategies. Gd_2O_3 nanopowders

doped with Eu^{3+} at varying concentrations and prepared by citrate gel as well as hydrothermal route, display cubic phase in the XRD analysis. Meanwhile solid state mixing- cum- sintering led Eu^{3+} doped orthovanadate nanosystem exhibited zircon type crystal structure. Occurrence of no extra peak suggests that Eu_2O_3 and $EuVO_4$ phase is not formed separately in EuGNP and EuGdV nanosystems respectively. TEM imaging allowed us to visualize the nanocrystalline feature along with the indication of amorphous surface layer due to citric acid coating in GNP and 3% EuGNP. From the SAED patterns a perfect periodicity could be assumed following the concentric ring-type patterns along with distinct bright spots. The interplanar spacing as determined from TEM imaging features estimated to be, ~0.28 nm, 0.29 nm and ~0.3 nm, corroborate with the (400), (200) and (222) planes respectively. A noticeable reduction in the spacing between successive planes can be realized due to the inclusion of Eu^{3+} into the Gd_2O_3 host. The TEM imaging of GdV and 3% EuGdV clearly reveals clumps of spherical $GdVO_4$ nanoparticles. While the SAED pattern of GdV reveals diffused ring pattern, prominent rings can be observed in case of 3% EuGdV thereby confirming polycrystalline nature of the specimens. The interplanar distances as measured from the lattice fringes corresponded to (200) and (312) planes of GdV and 3% EuGdV respectively and are in good agreement with the XRD results.

The optical band gap of the as prepared nanosytem are determined from the absorbance spectra using Kubleka-Munk method. In the present case they are estimated as, ~5.3 eV and ~3.5eV as for Gd based oxides and vanadate systems respectively. The band gaps and phonon absorption energies for the undoped GNP and Eu:GNP systems, are also predicted through Kumar's model. Following the XPS based study of GNP and EuGNP nanosystems, the valance band maximum is determined to be ~8.4 eV. Upon Eu inclusion as dopant, peaks at ~1137 eV and ~1152 eV can be observed, which characterize +3 and +2 oxidation states of Eu, respectively. This important observation of_the signal from +2 oxidation state of Eu, is attributed to 'surface valence transition' involved in the

system. The XPS study also suggests that for 3% doped EuGNP the interaction between the Gd-orbitals with that of the surrounding Eu is believed to be higher as compared to other cases. Spin splitting can be witnessed from the Gd*4d* spectra and contribution of spin polarization to the profile is found to be greater in the case of doped system, due to sufficient overlap in the wavefunctions of Eu and Gd along with spin coupling. Such observations have not yet been discussed for Eu doped RE oxides in the available reports. The effect of introduction of Eu^{3+} dopant into the vanadate matrix was also studied in great detail. A weak peak at ~1137 eV has been witnessed in the XPS spectra for 3% EuGdV, describing +3 oxidation state of europium in the $GdVO_4$ lattice. No observations were made that suggest +2 oxidation state of Eu dopant in the lattice host as observed in oxide based system.

Bibliography

[1] Hazarika, S. and Mohanta, D., Production and optoelectronic response of Tb 3+ activated gadolinium oxide nanocrystalline phosphors. *The European Physical Journal-Applied Physics*, 62(3), 2013.

[2] Hazarika, S., Paul, N., and Mohanta, D., Rapid hydrothermal route to synthesize cubic-phase gadolinium oxide nanorods. *Bulletin of Materials Science*, 37(4):789-796, 2014.

[3] Dhananjaya, N., Nagabhushana, H., Nagabhushana, B., Chakradhar, R., Shivakumara, C., and Rudraswamy, B., Synthesis, characterization and photoluminescence properties of Gd_2O_3:Eu^{3+} nanophosphors prepared by solution combustion method. *Physica B: Condensed Matter*, 405(17):3795-3799, 2010.

[4] JCPDS-ICCD, P.D.F., Joint Committee On Powder Diffraction Standards. *International Center for Diffraction Data*, Pennsylvania, USA, 2001.

[5] Park, J.Y., Baek, M.J., Choi, E.S., Woo, S., Kim, J.H., Kim, T.J., Jung, J.C., Chae, K.S., Chang, Y., and Lee, G.H., Paramagnetic ultrasmall gadolinium oxide nanoparticles as advanced T 1 MRI contrast agent: account for large longitudinal relaxivity, optimal particle diameter, and in vivo T 1 MR images. *ACS Nano*, 3(11):3663-3669, 2009.

[6] Mukherjee, S., Dasgupta, P., and Jana, P.K., Size-dependent dielectric behaviour of magnetic Gd_2O_3 nanocrystals dispersed in a silica matrix. *Journal of Physics D: Applied Physics*, 41(21):215004, 2008.

[7] Kumar, V., Sharma, S.K., Sharma, T., and Singh, V., Band gap determination in thick films from reflectance measurements. *Optical Materials*, 12(1):115-119, 1999.

[8] Kuznetsova, Y.A. and Zatsepin, A. Optical properties and energy parameters of Gd_2O_3 and Gd_2O_3: Er nanoparticles. in *Journal of Physics: Conference Series*, Vol. 917. 062001: IOP Publishing, 2017.

[9] Wakaki, M., Shibuya, T., and Kudo, K. *Physical properties and data of optical materials*. CRC press, 2018.

[10] Foix, D., Martinez, H., Pradel, A., Ribes, M., and Gonbeau, D., XPS valence band spectra and theoretical calculations for investigations on thiogermanate and thiosilicate glasses. *Chemical Physics*, 323(2-3):606-616, 2006.

[11] Tougaard, S. and Chorkendorff, I., Differential inelastic electron scattering cross sections from experimental reflection electron-energy-loss spectra: Application to background removal in electron spectroscopy. *Physical Review B*, 35(13):6570, 1987.

[12] Zatsepin, D., Galakhov, V., Korotin, M., Fedorenko, V., Kurmaev, E., Bartkowski, S., Neumann, M., and Berger, R., Valence states of copper ions and electronic structure of LiCu 2 O 2. *Physical Review B*, 57(8):4377, 1998.

[13] Barreca, D., Gasparotto, A., Milanov, A., Tondello, E., Devi, A., and Fischer, R.A., Gd2O3 nanostructured thin films analyzed by XPS. *Surface Science Spectra*, 14(1):60-67, 2007.

[14] Zhou, J.-P., Chai, C.-L., Yang, S.-Y., Liu, Z.-K., Song, S.-L., Li, Y.-L., and Chen, N.-F., Properties of high k gate dielectric gadolinium oxide deposited on Si (1 0 0) by dual ion beam deposition (DIBD). *Journal of Crystal Growth*, 270(1-2):21-29, 2004.

[15] Shirley, D.A., High-resolution X-ray photoemission spectrum of the valence bands of gold. *Physical Review B*, 5(12):4709, 1972.

[16] Kumar, S., Prakash, R., Choudhary, R., and Phase, D., Structural, XPS and magnetic studies of pulsed laser deposited Fe doped Eu2O3 thin film. *Materials Research Bulletin*, 70:392-396, 2015.

[17] Mercier, F., Alliot, C., Bion, L., Thromat, N., and Toulhoat, P., XPS study of Eu (III) coordination compounds: Core levels binding energies in solid mixed-oxo-compounds $Eu_mX_xO_y$. *Journal of Electron Spectroscopy and Related Phenomena*, 150(1):21-26, 2006.

[18] Cho, E.-J. and Oh, S.-J., Surface valence transition in trivalent Eu insulating compounds observed by photoelectron spectroscopy. *Physical Review B*, 59(24):R15613, 1999.

[19] Bae, J., Park, S., Hong, T., Kim, J., Yoon, J., Jeong, E., Won, M., and Jeong, J., Optical and surface analysis of lithium incorporated GdVO4: Eu3+ phosphor powders. *Current Applied Physics*, 9(3):S241-S244, 2009.

[20] Osawa, S., Katsumata, T., Iyoda, T., Enoki, Y., Komuro, S., and Morikawa, T., Effects of composition on the optical properties of doped and nondoped $GdVO_4$. *Journal of Crystal Growth*, 198:444-448, 1999.

[21] Jovanović, D.J., Chiappini, A., Zur, L., Gavrilović, T.V., Tran, T.N.L., Chiasera, A., Lukowiak, A., Smits, K., Dramićanin, M.D., and Ferrari, M., Synthesis, structure and spectroscopic properties of luminescent $GdVO_4$:Dy^{3+} and $DyVO_4$ particles. *Optical Materials*, 76:308-316, 2018.

[22] Ryu, S.-M. and Nam, C., Effects of annealing on nanocrystalline $GdVO_4$ and its magnetocaloric properties. Applied Physics A, 126:1-8, 2020.

[23] Xu, Z., Feng, B., Gao, Y., Zhao, Q., Sun, D., Gao, X., Li, K., Ding, F., and Sun, Y., Uniform and well-dispersed $GdVO_4$ hierarchical architectures: hydrothermal synthesis, morphology evolution, and luminescence properties. *CrystEngComm*, 14(17):5530-5538, 2012.

[24] Szczeszak, A., Grzyb, T., Śniadecki, Z., Andrzejewska, N., Lis, S., Matczak, M., Nowaczyk, G., Jurga, S., and Idzikowski, B., Structural, spectroscopic, and magnetic properties of Eu^{3+}-doped GdVO4 nanocrystals synthesized by a hydrothermal method. *Inorganic Chemistry*, 53(23):12243-12252, 2014.

[25] Tang, S., Huang, M., Wang, J., Yu, F., Shang, G., and Wu, J., Hydrothermal synthesis and luminescence properties of GdVO4: Ln3+ (Ln= Eu, Sm, Dy) phosphors. *Journal of Alloys and Compounds*, 513:474-480, 2012.

[26] Yan, B. and Wu, J.-H., Solid state-hydrothermal synthesis and photoluminescence of LaVO4: Eu3+ nanophosphors. *Materials Letters*, 63(11):946-948, 2009.

[27] Gschneidner, K.A., Bunzli, J.-C.G., and Pecharsky, V.K. *Handbook on the physics and chemistry of rare earths: optical spectroscopy*. Elsevier, 2011.

[28] Kang, J.H., Im, W.B., Lee, D.C., Kim, J.Y., Jeon, D.Y., Kang, Y.C., and Jung, K.Y., Correlation of photoluminescence of (Y, Ln) VO_4: Eu^{3+} (Ln= Gd and La) phosphors with their crystal structures. *Solid State Communications*, 133(10):651-656, 2005.

[29] Singh, N.S., Ningthoujam, R., Devi, L.R., Yaiphaba, N., Sudarsan, V., Singh, S.D., Vatsa, R., and Tewari, R., Luminescence study of Eu^{3+} doped $GdVO_4$ nanoparticles: Concentration, particle size, and core/shell effects. *Journal of Applied Physics*, 104(10):104307, 2008.

[30] Baglio, J.t. and Sovers, O., Crystal structures of the rare-earth orthovanadates. *Journal of Solid State Chemistry*, 3(3):458-465, 1971.

[31] Mahapatra, S. and Ramanan, A., Hydrothermal synthesis and structural study of lanthanide orthovanadates, $LnVO_4$ (Ln= Sm, Gd, Dy and Ho). *Journal of Alloys and Compounds*, 395(1-2):149-153, 2005.

[32] Carbonati, T., Cionti, C., Cosaert, E., Nimmegeers, B., Meroni, D., and Poelman, D., NIR emitting $GdVO_4$:Nd nanoparticles for bioimaging: The role of the synthetic pathway. *Journal of Alloys and Compounds*, 862:158413, 2021.

[33] He, Y., Cai, J., Li, T., Wu, Y., Lin, H., Zhao, L., and Luo, M., Efficient degradation of RhB over $GdVO_4$/g-C_3N_4 composites under visible-light irradiation. *Chemical Engineering Journal*, 215:721-730, 2013.

[34] Su, X., Yan, B., and Huang, H., In situ co-precipitation synthesis and luminescence of $GdVO_4$:Eu^{3+} and $Y_xGd_{1-x}VO_4$:Eu^{3+} microcrystalline phosphors derived from the assembly of hybrid precursors. *Journal of Alloys and Compounds*, 399(1-2):251-255, 2005.

[35] Zhang, Q.-l., Guo, C.-x., Shi, C.-s., and Lü, S.-z., High-resolution photoluminescence spectrum of $GdVO_4$:Eu^{3+}. *Journal of Alloys and Compounds*, 309(1-2):10-15, 2000.

[36] Ronde, H. and Blasse, G., The nature of the electronic transitions of the vanadate group. *Journal of Inorganic and Nuclear Chemistry*, 40(2):215-219, 1978.

[37] Nakajima, T., Isobe, M., Tsuchiya, T., Ueda, Y., and Manabe, T., Correlation between luminescence quantum efficiency and structural properties of vanadate phosphors with chained, dimerized, and isolated VO_4 tetrahedra. *The Journal of Physical Chemistry C*, 114(11):5160-5167, 2010.

[38] Ronde, H. and Snijder, J., The position of the VO_4^{3-} charge-transfer transition as a function of the V- O distance. *Chemical Physics Letters*, 50(2):282-283, 1977.

[39] Geng, D., Cabello-Olmo, E., Lozano, G., and Míguez, H., Photonic structuring improves the colour purity of rare-earth nanophosphors. *Materials horizons*, 5(4):661-667, 2018.

[40] Riwotzki, K. and Haase, M., Wet-chemical synthesis of doped colloidal nanoparticles: YVO_4:Ln (Ln= Eu, Sm, Dy). *The Journal of Physical Chemistry B*, 102(50):10129-10135, 1998.

[41] Yang, L., Li, G., Zhao, M., Zheng, J., Guan, X., and Li, L., Morphology-controllable growth of $GdVO_4$:Eu^{3+} nano/microstructures for an optimum red luminescence. *Nanotechnology*, 23(24):245602, 2012.

[42] Xu, Z., Kang, X., Li, C., Hou, Z., Zhang, C., Yang, D., Li, G., and Lin, J., Ln3+ (Ln= Eu, Dy, Sm, and Er) ion-doped YVO4 nano/microcrystals with multiform morphologies: hydrothermal synthesis, growing mechanism, and luminescent properties. *Inorganic Chemistry*, 49(14):6706-6715, 2010.

[43] Dolgos, M.R., Paraskos, A.M., Stoltzfus, M.W., Yarnell, S.C., and Woodward, P.M., The electronic structures of vanadate salts: cation substitution as a tool for band gap manipulation. *Journal of Solid State Chemistry*, 182(7):1964-1971, 2009.

[44] Jovanović, D.J., Antić, Ž., Krsmanović, R.M., Mitrić, M., Đorđević, V., Bártová, B., and Dramićanin, M.D., Annealing effects on the microstructure and photoluminescence of Eu^{3+}-doped $GdVO_4$ powders. *Optical Materials*, 35(10):1797-1804, 2013.

[45] Mialon, G., Turkcan, S., Alexandrou, A., Gacoin, T., and Boilot, J.-P., New insights into size effects in luminescent oxide nanocrystals. *The Journal of Physical Chemistry C*, 113(43):18699-18706, 2009.

[46] Klochkov, V., Comparative analysis of photocatalytic activity of aqueous colloidal solutions of $ReVO_4$:Eu^{3+} (Re= La, Gd, Y), $CePO_4$: Tb, CeO_2 and C_{60}. Journal of Photochemistry and Photobiology A: Chemistry, 310:128-133, 2015.

[47] Zheng, F., Wang, W., and Yang, P., $GdVO_4$: Ln^{3+} (Ln= Eu, Dy, and Sm) microstructures: solvothermal and luminescent properties. *Optoelectronics and Advanced Materials-Rapid Communications*, 5(June 2011):596-599, 2011.

[48] Gupta, J., Landheer, D., McCaffrey, J., and Sproule, G., Gadolinium silicate gate dielectric films with sub-1.5 nm equivalent oxide thickness. *Applied Physics Letters*, 78(12):1718-1720, 2001.

[49] Molle, A., Wiemer, C., Bhuiyan, M.N.K., Tallarida, G., Fanciulli, M., and Pavia, G., Cubic-to-monoclinic phase transition during the epitaxial growth of crystalline Gd_2O_3 films on Ge (001) substrates. *Applied Physics Letters*, 90(19):193511, 2007.

[50] Wagner, C., Naumkin, A., Kraut-Vass, A., Allison, J., Powell, C., and Rumble Jr, J., NIST standard reference database 20, Version 3.4 (Web version). *National Institute of Standards and Technology: Gaithersburg*, MD, 20899, 2003.

[51] Biesinger, M.C., Lau, L.W., Gerson, A.R., and Smart, R.S.C., Resolving surface chemical states in XPS analysis of first row transition metals, oxides and hydroxides: Sc, Ti, V, Cu and Zn. *Applied Surface Science*, 257(3):887-898, 2010.

[52] Shandilya, P., Mittal, D., Sudhaik, A., Soni, M., Raizada, P., Saini, A.K., and Singh, P., $GdVO_4$ modified fluorine doped graphene nanosheets as dispersed photocatalyst for mitigation of phenolic compounds in aqueous environment and bacterial disinfection. *Separation and Purification Technology*, 210:804-816, 2019.

[53] Kim, D., Jin, Y.-H., Jeon, K.-W., Kim, S., Kim, S.-J., Han, O.H., Seo, D.-K., and Park, J.-C., Blue-silica by Eu 2+-activator occupied in interstitial sites. *RSC Advances*, 5(91):74790-74801, 2015.